

## Electronic Supplementary Information

### **Imaging cervical cytology with scanning near-field optical microscopy (SNOM) coupled with an IR-FEL**

Diane E. Halliwell,<sup>a</sup> Camilo L. M. Morais,<sup>b</sup> Kássio M. G. Lima,<sup>b</sup> Júlio Trevisan,<sup>c</sup> Michele R. F. Siggel-King,<sup>de</sup> Tim Craig,<sup>d</sup> James Ingham,<sup>d</sup> David S. Martin,<sup>d</sup> Kelly A. Heys,<sup>a</sup> Maria Kyrgiou,<sup>f,g</sup> Anita Mitra,<sup>f,g</sup> Evangelos Paraskevaidis,<sup>h</sup> Georgios Theophilou,<sup>i</sup> Pierre L. Martin-Hirsch,<sup>aj</sup> Antonio Cricenti,<sup>k</sup> Marco Luce,<sup>k</sup> Peter Weightman,<sup>d</sup> and Francis L. Martin<sup>a,l</sup>

<sup>a</sup>*Centre for Biophotonics, LEC, Lancaster University, Lancaster, UK;* <sup>b</sup>*Biological Chemistry and Chemometrics, Institute of Chemistry, Federal University of Rio Grande do Norte, Natal 59072-970, RN, Brazil;* <sup>c</sup>*Institute of Astronomy, Geophysics and Atmospheric Sciences, University of São Paulo, Brazil;* <sup>d</sup>*Department of Physics, University of Liverpool, Oliver Lodge Building, Liverpool, UK;* <sup>e</sup>*Accelerator Science and Technology Centre (ASTEC), STFC Daresbury Laboratory, UK;* <sup>f</sup>*Institute of Reproductive and Developmental Biology, Department of Surgery & Cancer, Faculty of Medicine, Imperial College, London, UK;* <sup>g</sup>*West London Gynaecological Cancer Centre, Imperial College NHS Healthcare, London, UK;* <sup>h</sup>*Department of Obstetrics and Gynaecology, University of Ioannina, Ioannina, Greece;* <sup>i</sup>*St James Hospital, Leeds, West Yorkshire, UK;* <sup>j</sup>*Department of Obstetrics and Gynaecology, Lancashire Teaching Hospitals NHS Trust Foundation, Preston, UK;* <sup>k</sup>*Istituto di Struttura della Materia, CNR, via del Fosso del Cavaliere 100, Rome, Italy;* <sup>l</sup>*School of Pharmacy and Biomedical Sciences, University of Central Lancashire, Preston, UK*

Number of Pages = 13

Number of Figures = 11

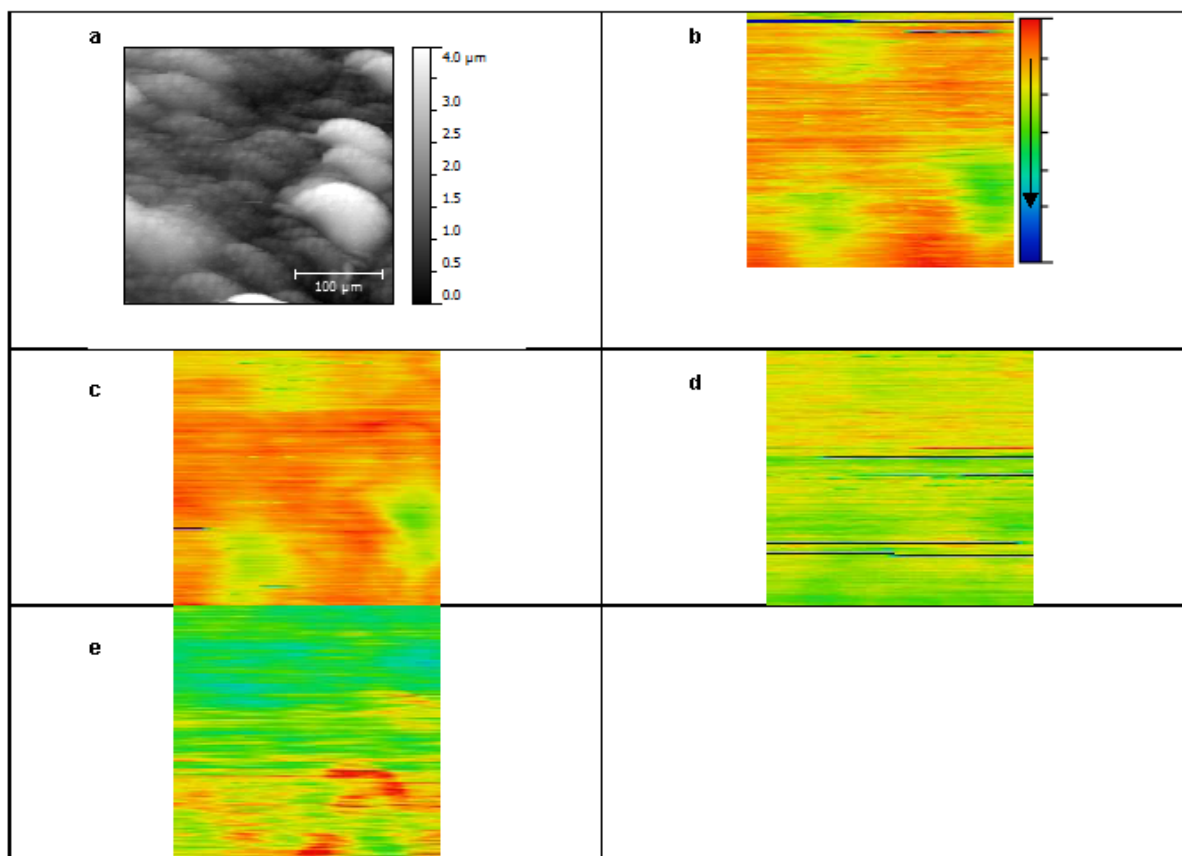


**Figure S1. SNOM-IR-FEL images of normal cells:** (a) topography; **transmission images:** (b) Amide I; (c) Amide II; (d) Lipids; and, (e) DNA. The colour scale bar arrow in (b) applies to (b-e) and indicates increasing biomarker absorption. SNOM-IR-FEL: Scanning near-field optical microscopy coupled with an infrared-free electron laser.

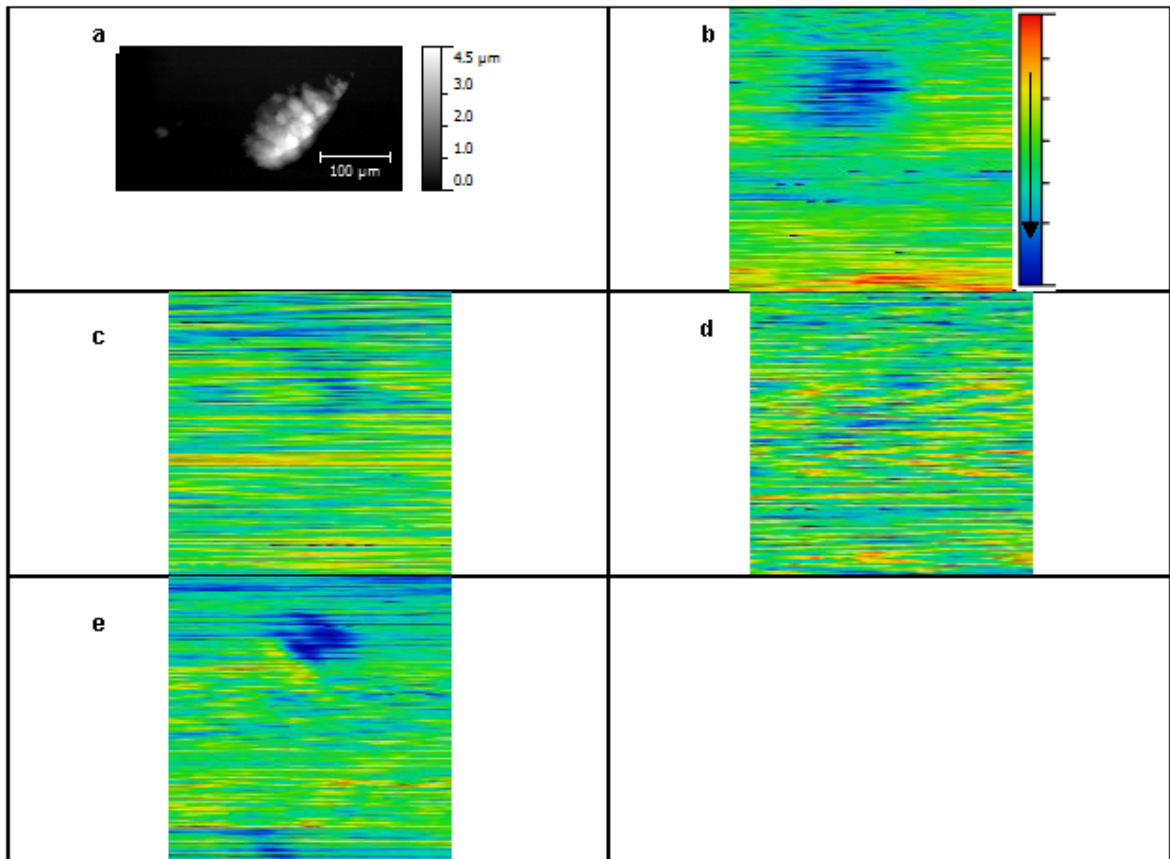


**Figure S2. SNOM-IR-FEL images of low-grade dyskaryosis: (a) topography; transmission images: (b) Amide I; (c) Amide II; (d) Lipids; and, (e) DNA. The colour scale bar arrow in (b) applies to (b-e) and indicates increasing biomarker absorption. SNOM-IR-FEL: Scanning near-field optical microscopy coupled with an infrared-free electron laser.**

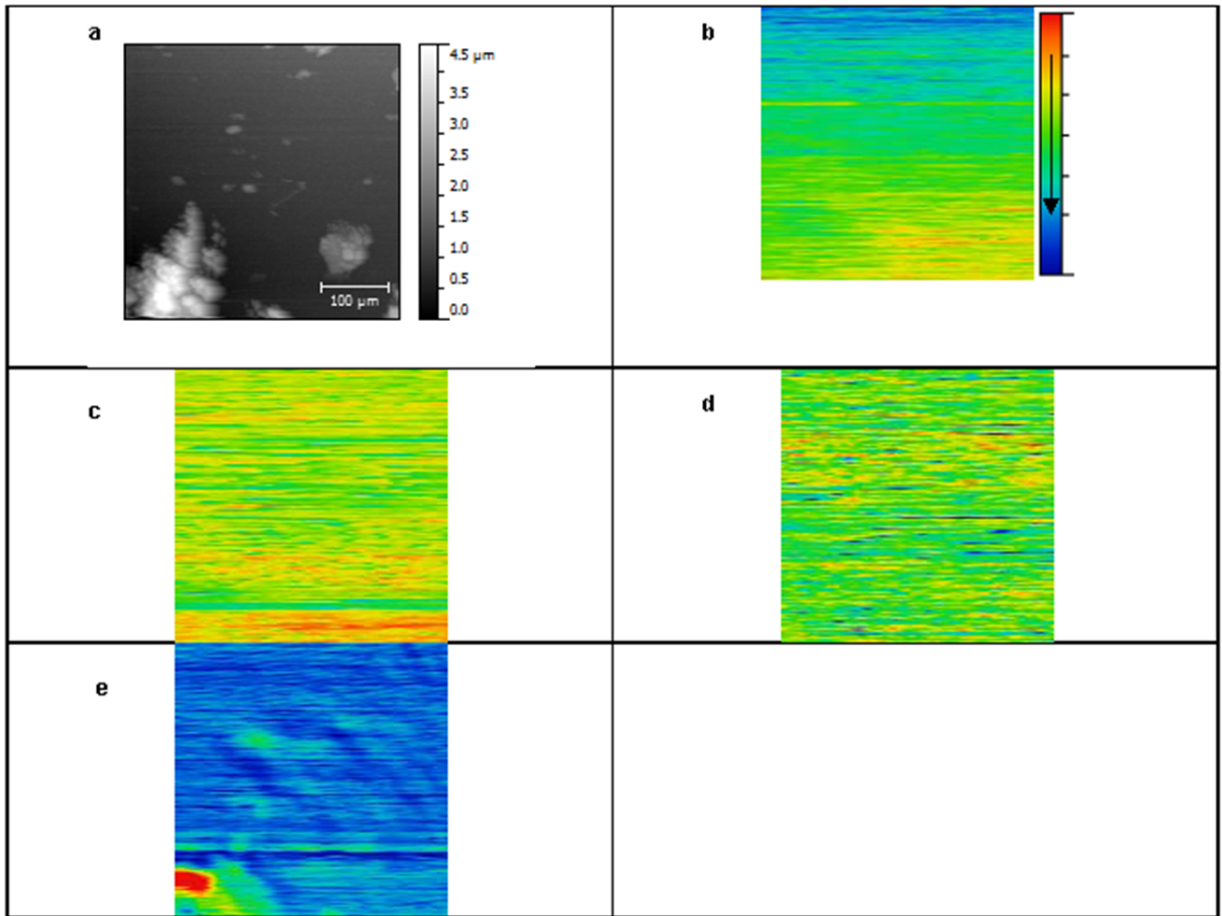


**Figure S3. SNOM-IR-FEL images of high-grade dyskaryosis: (a) topography; transmission images: (b) Amide I; (c) Amide II; (d) Lipids; and, (e) DNA. The colour scale bar arrow in (b) applies to (b-e) and indicates increasing biomarker absorption. SNOM-IR-FEL: Scanning near-field optical microscopy coupled with an infrared-free electron laser.**

The SNOM-IR-FEL images and associated topography of the pre-invasive lesion (CIN2, HGCGIN) are presented in the main body of the text (see Figure 6).

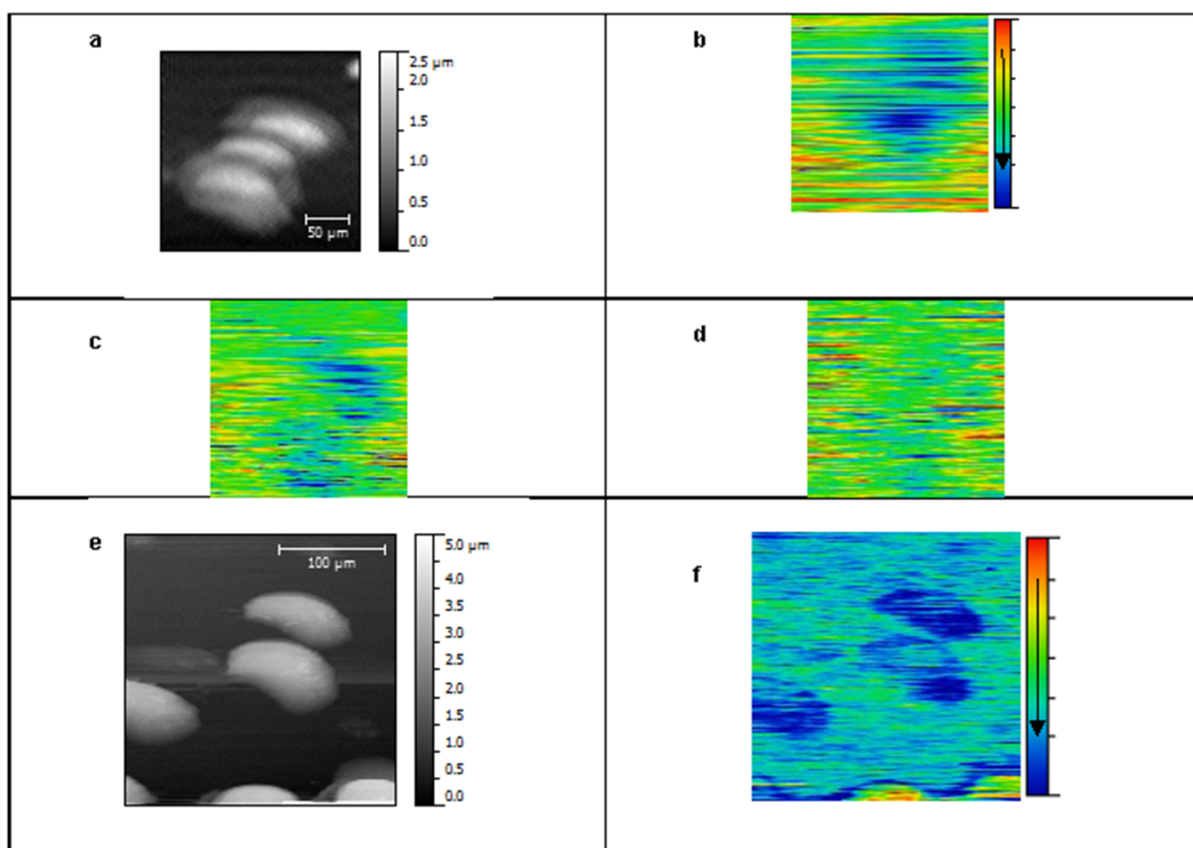


**Figure S4. SNOM-IR-FEL images of adenocarcinoma Stage 1B1:** (a) topography; **transmission images:** (b) Amide I (imaged from different site to topography shown here); (c) Amide II; and, (d) Lipids. (e) Topography of cells from a second area; and, (f) the corresponding SNOM transmission image for the DNA biomarker. The colour scale bar arrow in (b) applies to (b-d, f) and indicates increasing biomarker absorption. SNOM-IR-FEL: Scanning near-field optical microscopy coupled to an infrared-free electron laser.

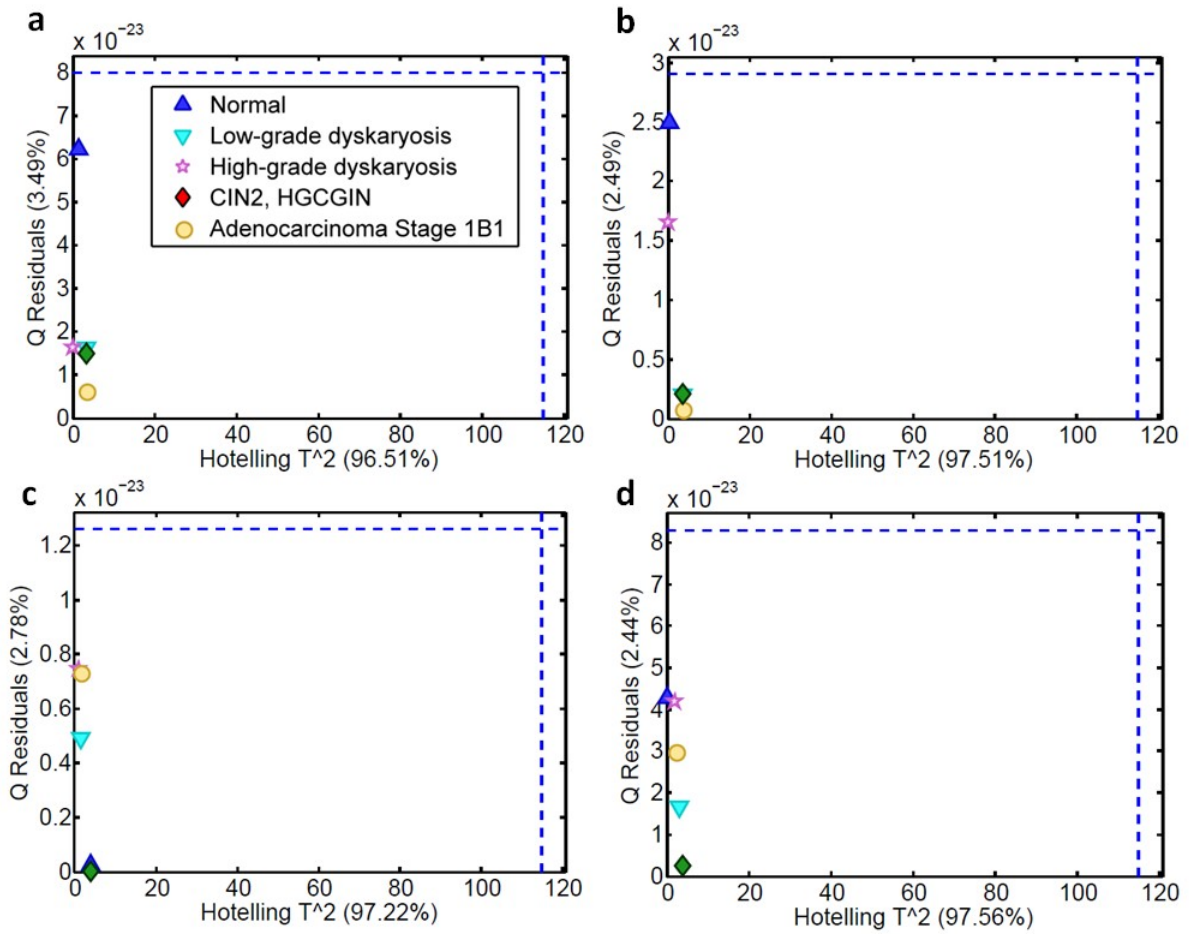


**Figure S5. Transmission SNOM-IR-FEL:** Hotelling  $T^2$  versus Q Residuals graphs for the type of cells according to each biomarker response: (a) Amide I; (b) Amide II; (c) Lipids; and, (d) DNA. All 5 samples fell within the 95% confidence limits (blue dotted line), and shows there were no outliers. The score for Hotelling  $T^2$  ranged from 96.51% to 97.56%; whilst the score for Q residuals ranged from 2.44% and 3.49%. CIN2, HGCGIN: Cervical intraepithelial neoplasia 2, high-grade cervical glandular intraepithelial neoplasia; SNOM-IR-FEL: Scanning near-field optical microscopy coupled with an infrared-free electron laser.

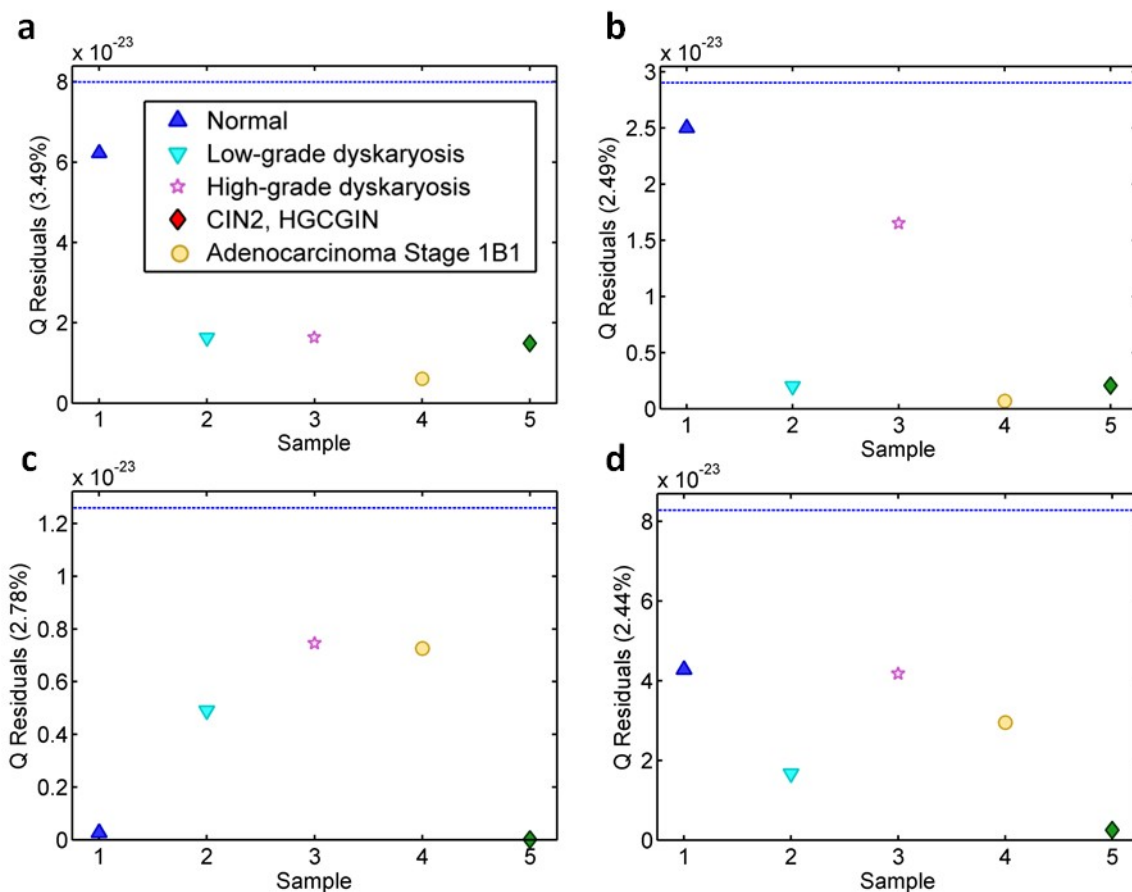


**Figure S6. Transmission SNOM-IR-FEL:** Validation of the PCA model using Q Residuals to measure variation outside the PCA model for each sample according each biomarker response: (a) Amide I; (b) Amide II; (c) Lipids; and, (d) DNA. The optimal score for Q Residuals is 0% and here ranged from 2.44% to 3.49%. All 5 samples fell within the 95% confidence limits (blue dotted line), shows there were no outliers and that the data fits the model well. CIN2, HGCGIN: Cervical intraepithelial neoplasia 2, high-grade cervical glandular intraepithelial neoplasia; SNOM-IR-FEL: Scanning near-field optical microscopy coupled with an infrared-free electron laser.

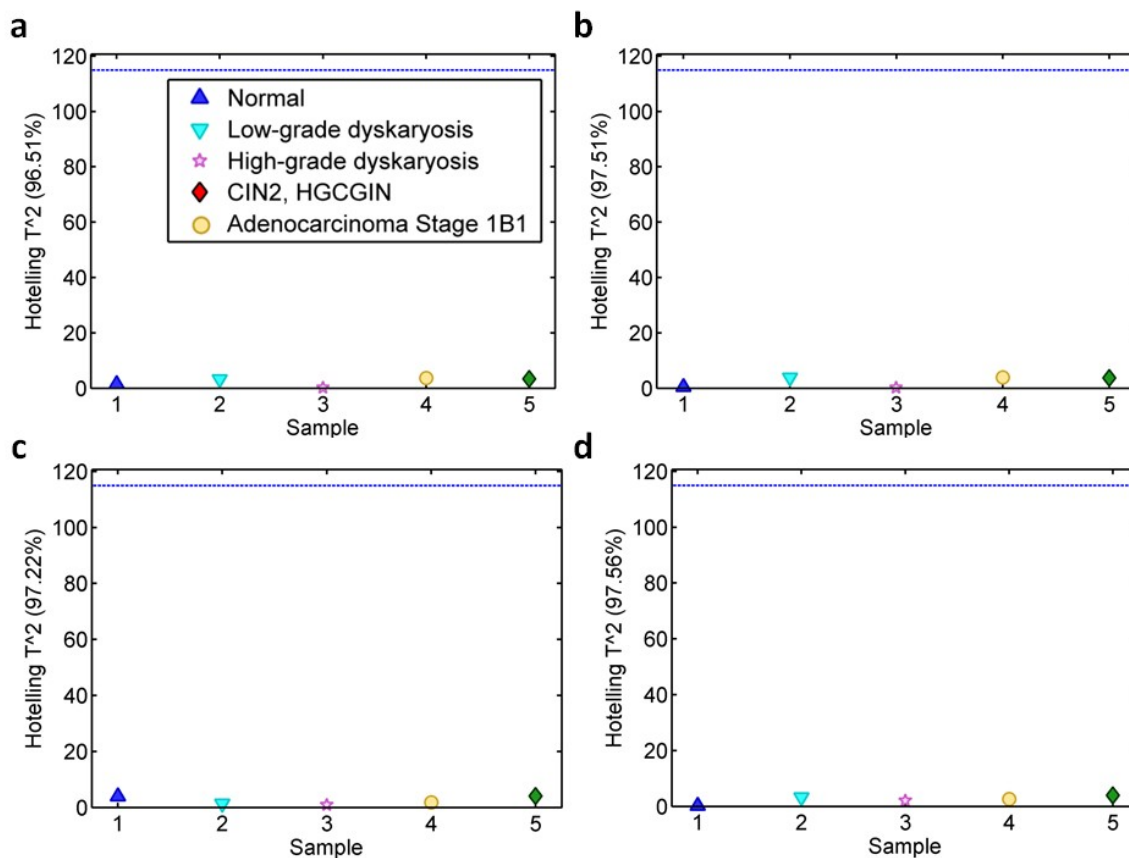


**Figure S7. Transmission SNOM-IR-FEL:** Validation of the PCA model using Hotelling  $T^2$  to measure variation within the PCA model for each sample according each biomarker response: (a) Amide I; (b) Amide II; (c) Lipids; and, (d) DNA. The optimal score for Hotelling  $T^2$  is 100% and here ranged from 96.51% to 97.56%. All 5 samples fell within the 95% confidence limits (blue dotted line), shows there were no outliers and that the data fits the model well. CIN2, HGCGIN: Cervical intraepithelial neoplasia 2, high-grade cervical glandular intraepithelial neoplasia; SNOM-IR-FEL: Scanning near-field optical microscopy coupled with an infrared-free electron laser.

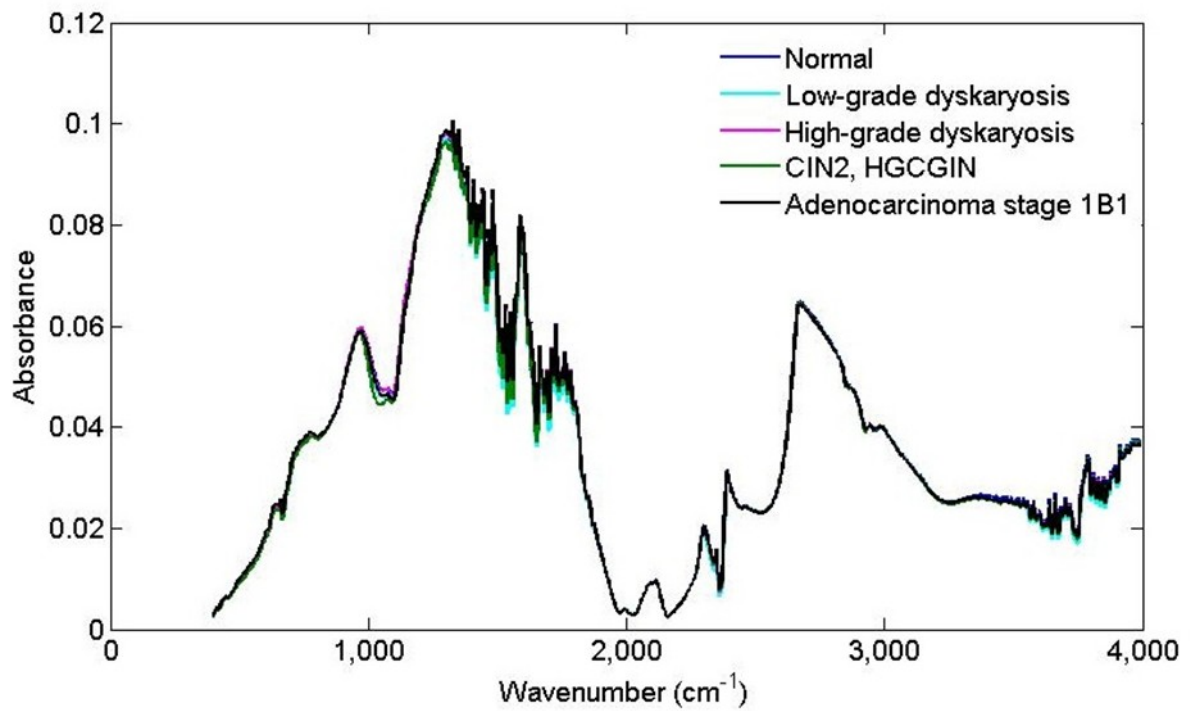


**Figure S8: ATR-FTIR spectroscopy:** Average infrared spectra of cell types.

ATR-FTIR spectroscopy: Attenuated total reflection Fourier-transform infrared spectroscopy; CIN2, HGCGIN: Cervical intraepithelial neoplasia 2, high-grade cervical glandular intraepithelial neoplasia.

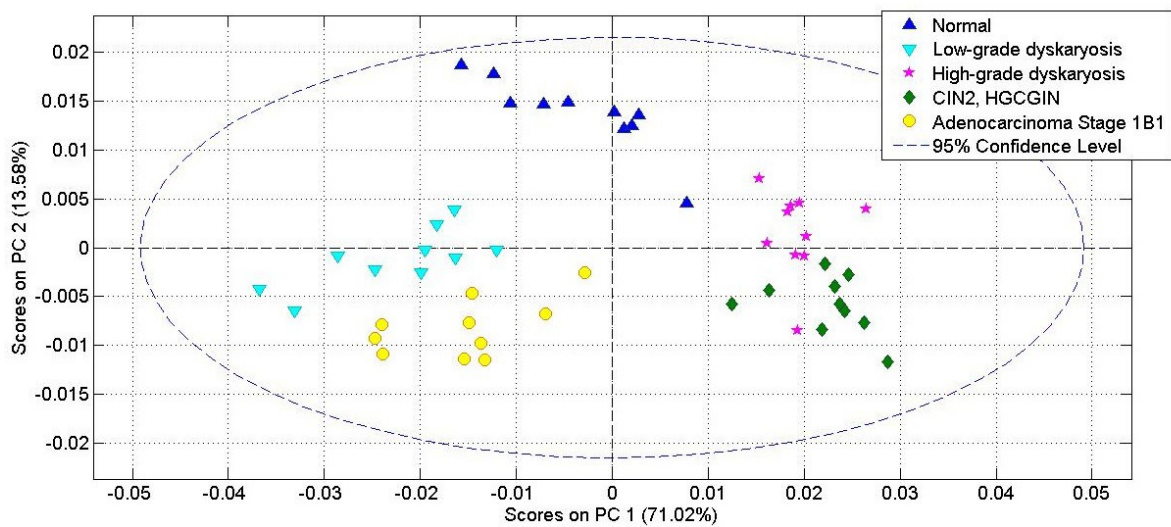


**Figure S9. ATR-FTIR spectroscopy:** Scores plot of 1<sup>st</sup> and 2<sup>nd</sup> principal components at a 95% confidence level. ATR-FTIR spectroscopy: Attenuated total reflection Fourier-transform infrared spectroscopy; CIN2, HGCGIN: Cervical intraepithelial neoplasia 2, high-grade cervical glandular intraepithelial neoplasia; principal components.

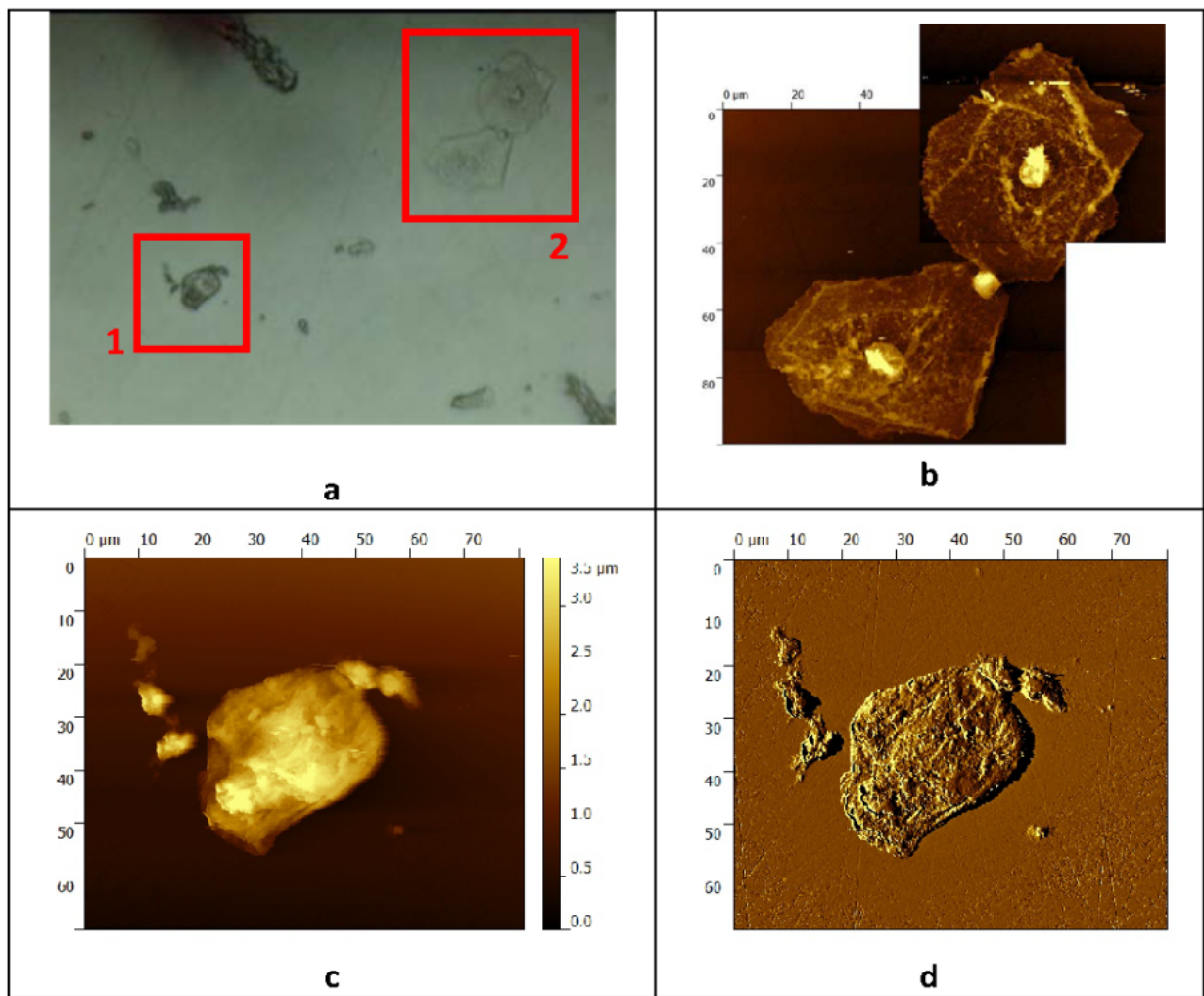


**Figure S10. AFM imaging of adenocarcinoma Stage 1B1:** (a) Optical image ( $\times 10$  magnification) identifying cells for investigation by AFM; and, (b) AFM topography image of two intermediate glandular cells [area 2 in (a)], the lower cell has two nuclei. The cells exhibit a long axis of  $\sim 75 \mu\text{m}$ . The cell thickness was measured at  $\sim 200 \text{ nm}$ , whereas the nuclei protruded  $\sim 1 \mu\text{m}$  in height from the substrate. (c) AFM topography; and, (d) deflection image of a cell identified [area 1 in (a)] as having a single enlarged nucleus separated from the rest of the cell by a halo. AFM: atomic force microscopy.

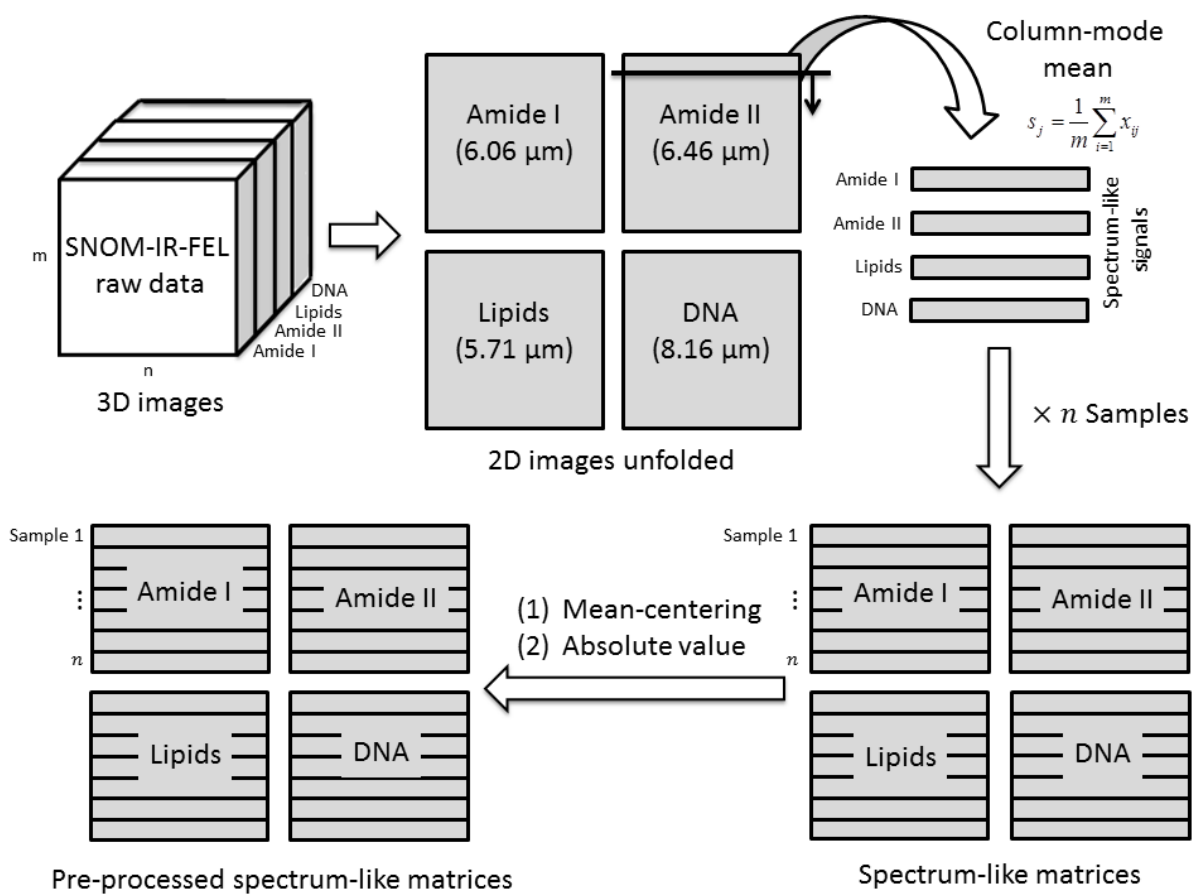


**Figure S11.** The computational steps taken in processing the data.